Impact of electrode kinetics on the dynamic response of a DMFC to change of methanol feed concentration

Thorsten Schultz [a], Ulrike Krewer [a], Kai Sundmacher [a,b,*]

[a] *Max Planck Institute for Dynamics of Complex Technical Systems, Sandtorstrasse 1, 39106 Magdeburg, Germany*
[b] *Otto-von-Guericke University Magdeburg, Process Systems Engineering, Universitätsplatz 2, 39106 Magdeburg, Germany*

Abstract

A dynamic one-dimensional rigorous process model of a single-cell direct methanol fuel cell (DMFC) is presented. Multi-component mass transport in the diffusion layers and the polymer electrolyte membrane (PEM) is described using the generalised Maxwell–Stefan equation for porous structures. In the PEM, local swelling behaviour and non-idealities are accounted for by a Flory–Huggins activity model. This model is used as basis of a model family with different anode and cathode reaction mechanisms (single-step and multi-step with and without adsorption to catalyst surface sites).

The model variants were used to simulate the dynamic (transient) response of the DMFC to stepwise changes in the methanol feed concentration from typical operating levels down to zero, while maintaining the cell current. For validation, similar experiments were carried out. In the experiments, the cell voltage broke down only after an unexpectedly long period of time, and for a variety of operating conditions even a cell voltage overshoot could be observed. Such overshoot behaviour is also predicted by those model variants, which feature anode reaction mechanisms with reaction intermediates (e.g. CO) adsorbed to the anode catalyst, while models without such detailed anode reaction mechanisms fail in this respect. The model-based analysis reveals that the observed overshoots result from the different time constants of the responses of the anode and cathode overpotentials to the feed change.

Keywords: Direct methanol fuel cell; Dynamic; Model; Electrode kinetics; Adsorption; Crossover

1. Introduction

The direct methanol fuel cell (DMFC) emerges as an interesting technology especially for portable power supply units. For such portable systems, dynamic rather than stationary operation is typical. But not only possibly rapid changes in the electrical power demand have to be considered, but also the fact that such

systems have to be quite simple, which, e.g. makes it difficult to keep the methanol feed concentration constant. Cheap and realiable sensors for methanol concentration are not available, and therefore a DMFC system will have to cope with changes in the methanol feed concentration, besides other operating conditions. Moreover, the examination of transient responses of a system to changes in the operating conditions can yield deeper insight into the governing internal physico-chemical phenomena.

In this work, the response of a DMFC to step changes in the methanol feed concentration is examined. Systematic experiments revealed a very interesting dynamic behaviour especially when the anode feed is changed from methanol solutions to pure water while maintaining the cell current. For low current densities, even intermediary increases in the cell voltage can be observed (overshoot behaviour) [1,2].

In order to understand the governing physico-chemical phenomena, a rigorous dynamic model of a DMFC was formulated. To find out the role of the anode and cathode reaction mech-

Nomenclature

a	activity
$a^*_{H_2O}$	water vapour activity
A^s	cell cross-sectional area (m^2)
B	transport matrix
c	molar concentration in fluid phase ($mol\,m^{-3}$)
$\tilde{c}$	molar pseudo-concentration w.r.t. total volume (in porous structures only) ($mol\,m^{-3}$)
d	thickness, diameter (m)
D	Maxwell–Stefan binary diffusion coefficient ($m^2\,s^{-1}$)
e	enthalpy flux density w.r.t. cross-sectional area A^s ($J\,m^{-2}\,s^{-1}$)
E^A	activation energy ($J\,mol^{-1}$)
F	Faraday's constant, $F = 96{,}485$ $A\,s\,mol^{-1}$ ($A\,s\,mol^{-1}$)
h	specific enthalpy ($J\,mol^{-1}$)
i	current density w.r.t. cross-sectional area A^S ($A\,m^{-2}$)
j	individual molar flux density w.r.t. cross-sectional area A^S ($mol\,m^{-2}\,s^{-1}$)
k	index for control volumes (discretised model)
L_i	friction terms ($s\,m^{-2}$)
m	mass flux density w.r.t. cross-sectional area A^S ($kg\,m^{-2}\,s^{-1}$)
M	molar mass ($kg\,mol^{-1}$)
n	overall molar flux density w.r.t. cross-sectional area A^S ($mol\,m^{-2}\,s^{-1}$)
N	number of moles (mol)
$N_{M,cu}$	number of chain units between two polymer cross-links
$\hat{N}$	mole density (loading) w.r.t. cross-sectional area A^S ($mol\,m^{-2}$)
$\hat{N}_{Pt}$	mole density of active Pt sites (anode/cathode catalyst) ($mol\,m^{-2}$)
p	pressure (Pa)
p_{sat}	saturation pressure (Pa)
q	heat flux density (due to thermal conduction) w.r.t. cross-sectional area A^S ($J\,m^{-2}\,s^{-1}$)
r	reaction rate w.r.t. total pore volume ($mol\,m^{-3}\,s^{-1}$)
R	ideal gas constant, $R = 8.314$ ($J\,mol^{-1}\,K^{-1}$)
t	time (s)
T	temperature (K)
U	voltage (V)
v	velocity ($m\,s^{-1}$)
V	volume (m^3)
V	molar volume ($m^3\,mol^{-1}$)
X	mole fraction in liquid phase
Y	mole fraction in gas phase
Z	cell coordinate perpendicular to cell plane
Z^*	number of transferred electrons/single charges

Greek symbols

α_a, α_c	charge transfer coefficients (anodic, cathodic)
ε	volume fraction (pore volume fraction = porosity)
η	overpotential (V)
η^{VIS}	dynamic viscosity (Pa s)
λ	thermal conductivity coefficient ($W\,m^{-1}\,K^{-1}$)
Λ	relative water content in membrane
μ	chemical potential ($J\,mol^{-1}$)
ν	stoichiometric coefficient
ϕ	electrical potential (V)
χ	non-ideality coefficient in Flory–Huggins activity model

Superscripts

A	anode compartment (supply channel structure)
AC	anode catalyst layer
ACP	polymer phase within (AC)
AD	anode diffusion layer
AF	anode feed
C	cathode compartment (supply channel structure)
CC	cathode catalyst layer
CCP	polymer phase within (CC)
CD	cathode diffusion layer
CF	cathode feed
eff	effective
M	membrane (PEM)
θ	at standard conditions: $T^\theta = 298$ K, $p^\theta = 10^5$ Pa

Subscripts

a	anode
c	cathode
carbon	carbon material
cell	cell
cu	polymer chain unit
CH_3OH	methanol
CO_2	carbon dioxide
eff	effective
H^+	proton
H_2O	water
i	counting index
j	counting index
Joule	Joule heating
N_2	nitrogen
O_2	oxygen
pores	in pore(s)
sat	saturated
sound	sound

anisms in the overall DMFC behaviour, assumed reaction mechanisms with different complexity were implemented in a base model. The base model features a very detailed description of mass transport phenomena, and has proven to be able to accurately predict steady state methanol and water crossover fluxes and cell voltages for a broad range of operating conditions [1,3,4].

Comparison of the simulation results obtained from the model variants reveals hints on the role of reaction intermediates on the platinum catalysts and methanol mass transport. It turns out, that intermediates adsorbed to the anode catalyst seem to play an important role, therefore an adequate dynamic model has to account for such phenomena. While similar mechanisms can be expected on the cathode catalyst as well (and are implemented in the most complex model variant), they seem to be of lower importance.

2. Dynamic experiments

Experiments were carried out using a single cell DMFC fed with air and liquid methanol water solutions. A detailed description of the DMFC design can be found in [1]. The identical anode and cathode monopolar plates are made from graphite material (thickness 7 mm, material code FU4369 by Schunk Kohlenstofftechnik, Germany). The flowbed structures consist of parallel channels of 2 mm width and 2 mm depth, with 1 mm wide ribs between them. The flowbed itself has the outer dimensions 65 mm × 40 mm (active area of $A^S = 26\,\text{cm}^2$). As diffusion layers PTFE-coated TORAY carbon paper (TGP-H-060) is used, with a PTFE loading between 20 and 25 mass% with respect to the uncoated material. The membrane electrode assemblies (MEA) are prepared from NAFION$^{\text{TM}}$ N-105 membrane foil, onto which the catalyst layers are applied using an airbrush technique. The anode catalyst layer features a catalyst loading of $5\,\text{mg cm}^{-2}$ (unsupported) platinum ruthenium black (Alfa Aesar Johnson Matthey HiSPEC$^{\text{TM}}$ 6000) and a NAFION$^{\text{TM}}$ content of 15 mass% relative to the metal loading (i.e. $0.75\,\text{mg cm}^{-2}$). The cathode catalyst layer has the same metal loading, but as catalyst (unsupported) platinum black is used (Alfa Aesar Johnson Matthey HiSPEC$^{\text{TM}}$ 1000) and the NAFION$^{\text{TM}}$ content is 10 mass% relative to the metal loading (i.e. $0.5\,\text{mg cm}^{-2}$).

In the experiments, the methanol feed concentration of the cell was changed stepwise from different starting values down to zero (pure water feed), while all other operating parameters (temperature, pressures, flow rates, etc.) of the cell as well as the cell current were kept constant. Some typical results of these experiments are presented in Fig. 1.
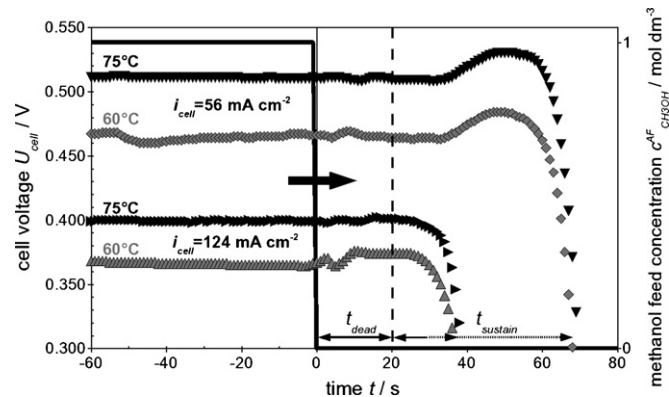
Fig. 1. Methanol feed concentration step-down experiments (galvanostatic operation) at different cell current densities and cell temperatures.

The full set of operating conditions is:

Anode
  Methanol feed concentration: $c_{\text{CH}_3\text{OH}}^{\text{AF}} = 1/1.5\,\text{mol dm}^{-3}$
  Pressure: $p^A = 1.7\,\text{bara} = 1.7 \times 10^5\,\text{Pa}$
  Feed flow rate: $F^{\text{AF}} = 0.5\,\text{dm}^3\,\text{min}^{-1}$
  Feed temperature: $T^A = 60/75/90\,^\circ\text{C}$
Cathode
  Dry air (dew point approximately $-2\,^\circ\text{C}$)
  Pressure: $p^C = 1.7\,\text{bara} = 1.7 \times 10^5\,\text{Pa}$
  Feed flow rate: $F^{\text{CF}} = 0.5\,\text{scbm h}^{-1}$ (at $1.013 \times 10^5\,\text{Pa}$ and $20\,^\circ\text{C}$)
  Feed temperature: $T^C = 30\,^\circ\text{C}$

As the feed switch is not located directly at the fuel cell inlet, a certain dead time occurs between the moment the valves are operated and the moment the changed feed solution reaches the anode inlet of the DMFC. This dead time depends on the anode feed flow rate. The distance between the feed switch valves and the anode inlet is approximately 6 m, with the pipes having an inner diameter of 6 mm. Assuming plug flow, this leads to a total dead volume of:

$$V_{\text{dead}} = A_{\text{pipe}}L_{\text{pipe}} = \frac{\pi}{4}d_{\text{pipe}}^2 L_{\text{pipe}}$$
$$= \frac{\pi}{4}(0.6\,\text{cm})^2 600\,\text{cm} = 170\,\text{cm}^3.$$

At the given flow rate of $500\,\text{cm}^3\,\text{min}^{-1}$ the dead time results as:

$$t_{\text{dead}} = \frac{V_{\text{dead}}}{F^{\text{AF}}} = \frac{170\,\text{cm}^3}{500\,\text{cm}^3\,\text{min}^{-1}} = 20\,\text{s}.$$

In Fig. 1, the dead time is marked by a vertical dashed line at 20 s after the feed switch. In all figures comparing experimental and simulation results, the dead time of the experiments is accounted for by substraction of 20 s from real time since switch, as in the model no such dead time is accounted for.

The dynamic response of the DMFC to step-down of the methanol feed concentration (Fig. 1) has two noteworthy features:

First, the cell voltage does not break down immediately after the switch to pure water feed, but only after some 10 s, depending on operating conditions. This is unexpected, as the feed flow rate is very high in the experiments, so that the mean residence time of the anode liquid in the anode flowbed compartment is below 1 s. Therefore one can assume, that the anode compartment as the supposedly main reservoir for fresh methanol is emptied completely within less than a second. Obviously there must be other reservoirs for reactants within the inner structures of the DMFC [1].

Second, for low current densities the inevitable cell voltage breakdown is not only taking place later than expected, but the cell voltage even shows an interim increase (overshoot behaviour) for low current densities ($<100\,\text{mA cm}^{-2}$). Such experimental behaviour was already reported elsewhere [2].

The results of the systematic experiments presented in Figs. 1–3 can be summarized as follows:
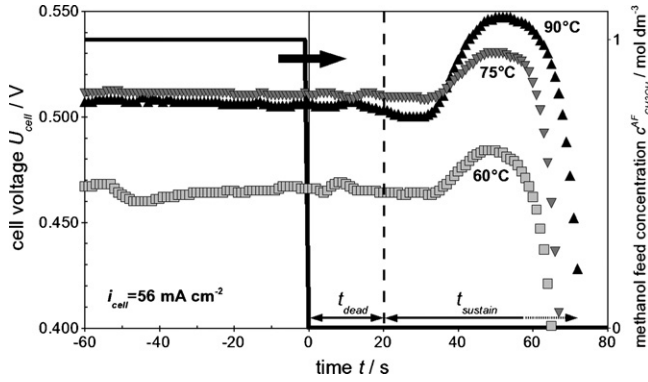
Fig. 2. Methanol feed concentration step-down experiments (galvanostatic operation) at different cell temperatures.

- In all cases (with or without overshooting), the cell breaks down much slower than the anode compartment is rinsed from methanol.
- The sustaining time $t_{sustain}$ (i.e. the time between end of dead time t_{dead} and the time the cell voltage has broken down to zero) is only a function of the cell current density, but not of the methanol feed concentration and cell temperature.
- Overshooting of the cell voltage only occurs for low current densities (Fig. 1).
- The higher the cell temperature, the higher the level of overshooting (Fig. 2).
- The higher the initial methanol feed concentration, the higher the level of overshooting (Fig. 3).
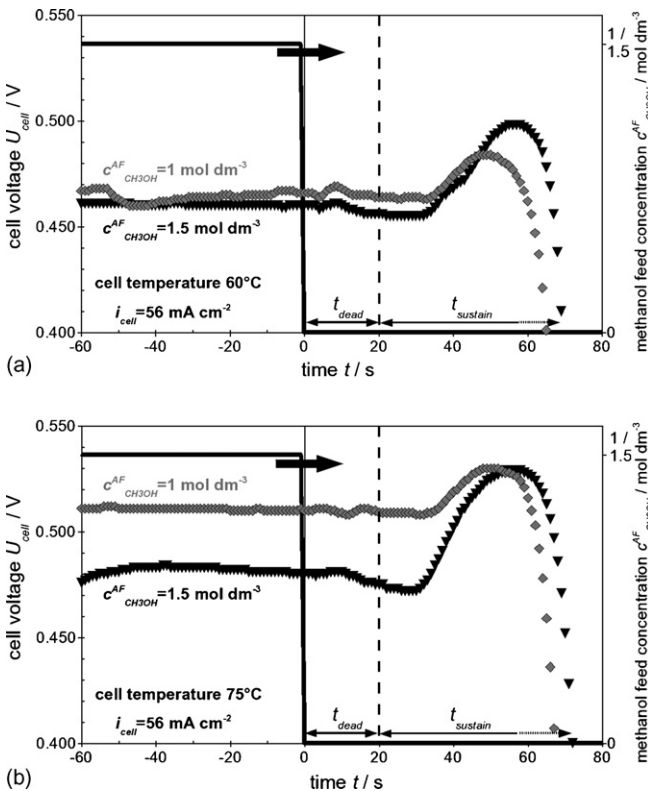
Fig. 3. Methanol feed concentration step-down experiments (galvanostatic operation) at different methanol feed concentrations and cell temperatures.

Explanations for this behaviour are based on the combination of several assumed physico-chemical phenomena occuring simultaneously in the DMFC:

- Methanol inside the pores of the anode diffusion layer and anode catalyst layer is not immediately rinsed out of the DMFC, therefore the methanol concentration in the anode catalyst layer is not decreasing as fast as that in the anode flowbed structure. As already shown elsewhere [1], this amount of methanol is too small to explain the observed sustaining times.
- Methanol inside the PEM could reverse its flow from cathode towards anode when the anode is completely rinsed, and thus supply the anode reaction with additional reactant.
- Reaction intermediates (e.g. CO) adsorbed to the anode catalyst are another possible reactant reservoir. If the supply of fresh methanol ceases, such intermediates could be fully oxidised, thus allowing further electric current flow.
- Decreased methanol crossover, due to decreasing methanol concentration in the anode catalyst layer, would lead to a decrease in the absolute cathode overpotential.

3. Model formulation

To analyse the experimental behaviour of the DMFC, a one-dimensional rigorous dynamic process model of a DMFC was developed [1,3,4]. It reflects the seven-layer structure of the DMFC: anode compartment (A), anode diffusion layer (AD), anode catalyst layer (AC), polymer electrolyte membrane (M), cathode catalyst layer (CC), cathode diffusion layer (CD) and cathode compartment (C). For all these layers, dynamic mass and energy balances, as well as quasi-steady state charge balances for (AC) and (CC) are formulated, and appropriate transport kinetics and internal boundary conditions are used to couple them. The diffusion layers and the PEM are spatially distributed elements, while the other four elements (catalyst layers and supply compartments) are described as ideally mixed systems. Fig. 4 presents a scheme of the model. The spatially distributed elements are described along the coordinates z^{AD}, z^M and z^{CD}, respectively, where the coordinates are perpendicular to the cell plane and increase from anode to cathode side. The model has proven to be capable of predicting measured steady state methanol and water crossover fluxes through the PEM under various operating conditions, with only one set of parameters [1,3]. For low to moderate current densities also the steady state current voltage characteristics are predicted with acceptable accuracy. A brief overview of all governing equations (balances, transport kinetics) is given in Table 1 (anode and cathode compartments, diffusion layers and catalyst layers) and Table 2 (PEM). The equations connected with the anode and cathode reaction kinetics (Table 3) will be discussed in more detail in the following sections. The symbols used in Tables 1–3 are explained in the list of symbols.

In this contribution, the model is used to simulate the dynamic response of the DMFC to changes in the methanol feed concentration. The analysis focuses on the role of the anode and cathode reaction kinetics, for which purpose several different reaction kinetic approaches for anode and cathode (Table 3) were imple-
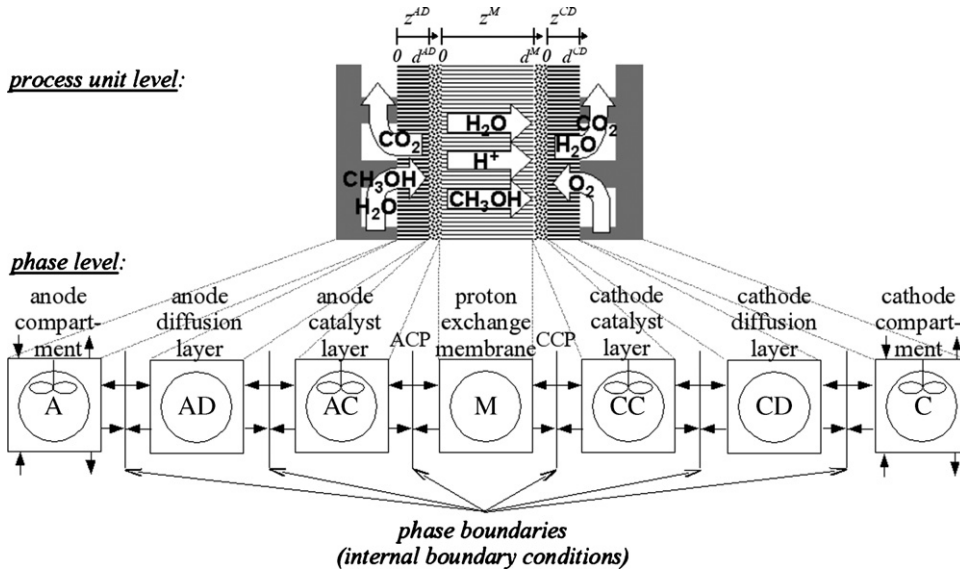
Fig. 4. Working pronciple of DMFC, model structure and geometry.

mented in the base model (Tables 1 and 2). The simulation results of these different model variants are then compared to experimental data in order to find out, which influence the electrode kinetics have on the overall dynamic behaviour of the DMFC. The final aim is to identify appropriate anode and cathode kinetic models, which can predict and physico-chemically explain the observed dynamic behaviour.

3.1. Model I: base model

In the base model (in the following referred to as model I), lumped reaction schemes are assumed [1,3]. Table 3 presents those reaction schemes (anode: T3.1; cathode: T3.12 and T3.13), the mass and charge balances (anode: T3.2 and T3.3; cathode: T3.14 and T3.15), and the corresponding rate expressions (anode: T3.4; cathode: T3.16 and T3.17).

The anodic methanol oxidation (Eq. T3.1) as well as the cathodic oxygen reduction (Eq. T3.12) are assumed to be reversible single-step electrochemical reactions, consequently their kinetics are decribed by classical Butler–Volmer approaches (Eqs. T3.4 and T3.16). At the cathode a second, undesired reaction takes place: methanol permeating through the PEM is oxidised to carbon dioxide (Eq. T3.13). It is assumed that this reaction is very fast, so that all methanol reaching the cathode is immediately consumed, independent of the electrode potential. Therefore, the rate of this reaction is proportional to the methanol flux reaching the cathode (Eq. T3.17).

The two reactions at the cathode are coupled via the component mass balances (Eq. T3.14) and also via the quasi-steady state charge balance (Eq. T3.15). The oxygen reduction consumes protons and electrons, while the methanol oxidation produces them, therefore the electric potential of the cathode is a mixed potential of both reactions' contributions.

3.2. Model II: extended anode kinetics

It is well known from DMFC literature that the anodic methanol oxidation on platinum ruthenium catalyst is neither a single-step nor a reversible reaction. It consists of various parallel and consecutive reaction and adsorption/desorption steps, with quite stable reaction intermediates bound to the different catalyst surfaces (usually platinum and ruthenium) [5]. Still the reaction mechanism is not fully understood and various possible mechanisms and corresponding rate expressions have been proposed, e.g.[5–8].

To account for the multi-step nature of the anodic methanol oxidation while limiting the complexity of the reaction scheme, a two-step mechanism is used here, which is a slightly simplified version of one that has been published recently [9]. It is presented in Table 3 (lower left quarter). In a first, irreversible step, methanol is adsorbed electrochemically to the platinum catalyst, forming strongly adsorbed carbon monoxide, four protons and four electrons (Eq. T3.5). The second step (T3.6) is a combination of three consecutive reactions: (a) water adsorbes electrochemically to the ruthenium catalyst in a fast and reversible reaction. (b) The formed Ru–OH then reacts irreversibly with the CO adsorbed on the adjacent platinum sites to carbon dioxide, two protons and two electrons. (c) Finally, the formed carbon dioxide desorbs from the electrode surface. In these three reaction steps, the irreversible reaction between adsorbed water and adsorbed CO (b) is assumed to be the rate determining step, while the water adsorption on ruthenium (a) is assumed to be always in quasi-equilibrium, and the carbon dioxide desorption (c) is assumed to be a fast and irreversible reaction.

Resulting from this reaction scheme, an additional component mass balance for the surface coverage of the platinum catalyst with CO (Θ_{CO}^{AC}, Eq. T3.8) is necessary, and the charge balance (T3.9) has to account for both reactions' charge productions.

As both combined reaction steps are irreversible electrochemical reactions, their rate expressions (Eqs. T3.10 and T3.11) are formulated as Tafel kinetics. Both reactions also include adsorption and desorption of species to the platinum catalyst surface, so the rate expressions also contain a term to

Table 1

Model equations and parameters of base model (flowbed compartments, diffusion layers and catalyst layers)

Components	Anode compartment (A)		Cathode compartment (C)	
	Index $j = H_2O$, CH_3OH, CO_2 (pure liquid phase)		Index $j = N_2$, O_2, H_2O, CO_2 (pure gas phase)	
Component mass balance	$\dfrac{dc_j^A}{dt} = \dfrac{1}{V^A}\{F^{AF}(c_j^{AF} - c_j^A) + A^s n_j^{AD}\vert_{z^{AD}=0}\}$	(T1.1)	$\dfrac{dc_j^C}{dt} = \dfrac{1}{V^C}(F^{CF}c_j^{CF} - F^C c_j^C + A^s n_j^{CD}\vert_{z^{CD}=d^{CD}})$	(Tl.13)
			with $F^C = F^{CF} + \dfrac{RT^C}{p^C}A^s \displaystyle\sum_j n_j^{CD}\vert_{z^{CD}=d^{CD}}$	(Tl.14)
Total mass balance	No balance, pressure p^A is operating parameter!		No balance, pressure p^C is operating parameter!	
Energy balance	No balance, temperature T^A is operating parameter!		No balance, temperatures T^C and T_{carbon}^C are operating parameters!	

Components	Anode diffusion layer (AD)		Cathode diffusion layer (CD)	
	Index $j = H_2O$, CH_3OH, CO_2 (pure liquid phase)		Index $j = N_2$, O_2, H_2O, CO_2 (pure gas phase)	
Component mass balance	$-c_{tot}^{AD}\dfrac{\partial x_j^{AD}}{\partial z} = \displaystyle\sum_{i \ne j}\dfrac{x_i^{AD}j_j^{AD} - x_j^{AD}j_i^{AD}}{\mathcal{D}_{ij}^{AD,eff}} + \dfrac{j_j^{AD}}{\mathcal{D}_{jM}^{AD,eff}}$	(T1.2)	$\dfrac{\partial c_j^{CD}}{\partial t} = \dfrac{1}{\varepsilon_{pores}^{CD}}\dfrac{\partial n_j^{CD}}{\partial z}$	(Tl.15)
Total mass balance	$\dfrac{\partial p^{AD}}{\partial t} = -(v_{sound}^{AD})^2\dfrac{\partial m_{tot}^{AD}}{\partial z}$	(Tl.3)	No balance, ideal gas:	
			$p^{CD} = \displaystyle\sum_j p_j^{CD} = RT^{CD}\sum_j c_j^{CD}$	(Tl.16)
Energy balance	$\dfrac{\partial T^{AD}}{\partial t} = -\dfrac{1}{(\widetilde{\rho c_p})^{AD}}\left(\dfrac{\partial e^{AD}}{\partial z} + \dfrac{\partial q^{AD}}{\partial z}\right)$	(Tl.4)	$\dfrac{\partial T^{CD}}{\partial t} = \dfrac{1}{(\widetilde{\rho c_p})^{CD}}\left[-\dfrac{\partial e^{CD}}{\partial z} - \dfrac{\partial q^{CD}}{\partial z}\right]$	(Tl.17)
	$(j^{AD}) = -\left(\displaystyle\sum_j c_j^{AD}\right)[B^{AD}]^{-1}\nabla(x^{AD})$		$(j^{CD}) = -\dfrac{1}{RT^{CD}}[B^{CD}]^{-1}\nabla(p^{CD})$	
Individual component flux densities (Maxwell–Stefan mass transport model)	with $B_{ii}^{AD} = \dfrac{1}{\mathcal{D}_{iM}^{AD,eff}} + \displaystyle\sum_{k \ne i}\dfrac{x_k^{AD}}{\mathcal{D}_{ik}^{AD,eff}}$, $B_{ij(i \ne j)}^{AD} = -\dfrac{x_i^{AD}}{\mathcal{D}_{ij}^{AD,eff}}$	(Tl.5)	with $B_{ii}^{CD} = \dfrac{1}{\mathcal{D}_{iM}^{CD,eff}} + \displaystyle\sum_{k \ne i}\dfrac{y_k^{CD}}{\mathcal{D}_{ik}^{CD,eff}}$, $B_{ij(i \ne j)}^{CD} = -\dfrac{y_i^{CD}}{\mathcal{D}_{ij}^{CD,eff}}$	(Tl.18)
Convective flow velocity	$v_p^{AD} = -\dfrac{(d_{pore}^{AD})^2}{32\eta^{vis}}\dfrac{\partial p^{AD}}{\partial z}$	(Tl.6)	$v_p^{CD} = -\dfrac{(d_{pore}^{CD})^2}{32\eta^{vis}}\dfrac{\partial p^{CD}}{\partial z}$	(Tl.19)
Total component flux densities	$n_j^{AD} = j_j^{AD} + \tilde{c}_j^{AD}v_p^{AD}$ with $\tilde{c}_j^{AD} = c_j^{AD}\varepsilon_{pores}^{AD}$	(Tl.7)	$n_j^{CD} = j_j^{CD} + \tilde{c}_j^{CD}v_p^{CD}$ with $\tilde{c}_j^{CD} = c^{CD}\varepsilon_{pores}^{CD}$	(Tl.20)
Total mass flux density	$m_{tot}^{AD} = \displaystyle\sum_j (n_j^{AD}\bar{M}_j)$	(Tl.8)	Not necessary as no total mass balance formulated	
Total enthalpy flux density	$e^{AD} = \displaystyle\sum_j (n_j^{AD}h_j(T^{AD}))$	(Tl.9)	$e^{CD} = \displaystyle\sum_j n_j^{CD}h_j(T^{CD})$	(Tl.21)
Conductive heat flow density	$q^{AD} = -\lambda^{AD,eff}\dfrac{\partial T^{AD}}{\partial z}$	(Tl.10)	$q^{CD} = -\lambda^{CD,eff}\dfrac{\partial T^{CD}}{\partial z}$	(Tl.22)

Components	Anode catalyst layer (AC)		Cathode catalyst layer (CC)	
	Index $j = H_2O$, CH_3OH, CO_2 (pure liquid phase)		Index $j = N_2$, O_2, H_2O, CO_2 (pure gas phase)	
Component mass balance	See individual model formulations!		See individual model formulations!	
Total mass balance	$\dfrac{dp^{AC}}{dt} = \dfrac{v_{sound}^2}{d^{AC}}(m_{tot}^M\vert_{z^M=0} - m_{tot}^{AD}\vert_{z^{AD}=d^{AD}})$	(Tl.11)	No balance, ideal gas law:	
			$p^{CC} = RT^{CC}\displaystyle\sum_j c_j^{CC}$	(Tl.23)
Energy balance	$\dfrac{dT^{AC}}{dt} = \dfrac{(e^M\vert_{z^M=0} - e^{AD}\vert_{z^{AD}=d^{AD}}) + (q^M\vert_{z^M=0} - q^{AD}\vert_{z^{AD}=d^{AD}})}{(\widetilde{\rho c_p})^{AC}d^{AC}}$	(Tl.12)	$\dfrac{dT^{CC}}{dt} = \dfrac{(e^{CD}\vert_{z^{CD}=0} - e^M\vert_{z^M=d^M}) + (q^{CD}\vert_{z^{CD}=0} - q^M\vert_{z^M=d^M})}{(\widetilde{\rho c_p})^{CC}d^{CC}}$	(Tl.24)
Charge balance	See individual model formulations!		See individual model formulations!	
Rate expressions	See individual model formulations!		See individual model formulations!	

Table 2

Model equations and parameters of base model (polymer electrolyte membrane)

Components	Polymer electrolyte membrane (M) Index j = H$_2$O, CH$_3$OH, (H$^+$) (pure liquid phase)			

Component mass balance

$$\frac{d\hat{N}_{j,k}^M}{dt} = n_{j,k}^M - n_{j,k+1}^M \quad \text{with} \quad \hat{N}_j = \frac{N_j}{A^S} \tag{T2.1}$$

Total mass balance

Pressures within membrane are not discussed!

Energy balance

$$\frac{\partial T^M}{\partial t} = \frac{1}{(\widetilde{\rho c_p})^M}\left[-\frac{\partial e^M}{\partial z} - \frac{\partial q^M}{\partial z} + i^M \frac{\partial \phi^M}{\partial z}\right] \tag{T2.2}$$

Total enthalpy flux density

$$e^M = \sum_j n_j^M h_j(T^M) \tag{T2.9}$$

Charge balance

$$0 = -\frac{\partial i^M}{\partial z} \tag{T2.3}$$

Conductive heat flow density

$$q^M = -\lambda^{M,\text{eff}}\frac{\partial T^M}{\partial z} \tag{T2.10}$$

Total component flux densities (Maxwell–Stefan mass transport model)

$$n_{H^+}^M = \frac{i^M}{F} = \frac{i_{\text{cell}}}{F} \tag{T2.4}$$

Electrical potential gradient

$$\frac{\partial \phi^M}{\partial z} = \frac{RT^M}{c_H^M, F}(L_{H^+} + n_{H^+}L_7 + n_{H_2O}L_8 + n_{CH_3OH}L_9) \tag{T2.11}$$

with $L_{H^+} = -\frac{c_{H^+}^M}{a_{H^+}^M}\frac{\partial a_{H^+}^M}{\partial z}$, $L_7 = \frac{x_{H_2O}}{\mathcal{D}_{H^+,H_2O}^{\textit{eff}}} + \frac{x_{CH_3OH}}{\mathcal{D}_{H^+,CH_3OH}^{\textit{eff}}} + \frac{1}{\mathcal{D}_{H^+,M}^{\textit{eff}}}$,

$L_8 = -\frac{x_{H^+}}{\mathcal{D}_{H^+,H_2O}^{\textit{eff}}}$, $L_9 = -\frac{x_{H^+}}{\mathcal{D}_{H^+,CH_3OH}^{\textit{eff}}}$

$$n_{CH_3OH}^M = \frac{L_{H_2O} + L_{CH_3OH} - n_{H^+}L_1 - n_{H_2O}L_2}{L_3} \tag{T2.5}$$

Activities (Flory–Huggins activity model)

$$a_j = \varepsilon_j \exp\left\{ \sum_{i \neq j}\left[\left(1 - \frac{\bar{V}_j}{\bar{V}_i}\right)\varepsilon_i + \chi_{j,i}\varepsilon_i^2\right] + \frac{\bar{V}_j}{2N_{M,cu}\bar{V}_{M,cu}}\varepsilon_M^{1/3}\right\}$$

with $\chi_{H_2O,M} = 0.7177$; $\chi_{CH_3OH,M} = 0.1348$; $\chi_{H_2O,CH_3OH} = 1.3$ (T2.12)

$$a_{H^+} = x_{H^+} \tag{T2.13}$$

$$n_{H_2O}^M = \frac{L_{H_2O} - n_{H^+}(L_4 - L_1L_6/L_3) - (L_2 + L_3)L_6/L_3}{L_5 - L_2L_6/L_3} \tag{T2.6}$$

with $L_{H_2O} = \frac{c_{H_2O}^M}{a_{H_2O}^M}\frac{\partial a_{H_2O}^M}{\partial z}$, $L_{CH_3OH} = -\frac{c_{CH_3OH}^M}{a_{CH_3OH}^M}\frac{\partial a_{CH_3OH}^M}{\partial z}$,

$L_1 = -\frac{x_{H_2O}}{\mathcal{D}_{H^+,H_2O}^{\textit{eff}}} - \frac{x_{CH_3OH}}{\mathcal{D}_{H^+,CH_3OH}^{\textit{eff}}}$ $L_2 = \frac{x_{H^+}}{\mathcal{D}_{H^+,H_2O}^{\textit{eff}}} + \frac{1}{\mathcal{D}_{H_2O,M}^{\textit{eff}}}$,

$L_3 = \frac{x_{H^+}}{\mathcal{D}_{H^+,CH_3OH}^{\textit{eff}}} + \frac{1}{\mathcal{D}_{CH_3OH,M}^{\textit{eff}}}$ $L_4 = -\frac{x_{H_2O}}{\mathcal{D}_{H^+,H_2O}^{\textit{eff}}}$,

$L_5 = \frac{x_{H^+}}{\mathcal{D}_{H^+,H_2O}^{\textit{eff}}} + \frac{x_{CH_3OH}}{\mathcal{D}_{H_2O,CH_3OH}^{\textit{eff}}} + \frac{1}{\mathcal{D}_{H_2O,M}^{\textit{eff}}}$ $L_6 = -\frac{x_{H_2O}}{\mathcal{D}_{H_2O,CH_3OH}^{\textit{eff}}}$,

Conversion of concentrations

$$\tilde{c}_{j,k}^M = \frac{\hat{N}_{j,k}^M}{\Delta z_k^M} \quad \text{with} \quad \Delta z_k^M = \frac{d^{M,\text{dry}}}{\text{ncv}^M} + \sum_j (\hat{N}_{j,k}^M \bar{V}_j) \tag{T2.14}$$

$$\varepsilon_j^M = \tilde{c}_j^M \bar{V}_j \tag{T2.15}$$

$$c_j^M = \frac{\tilde{c}_j^M}{\varepsilon_{\text{pores}}^M} \quad \text{with} \quad \varepsilon_{\text{pores}}^M = \sum_j \varepsilon_j^M = \varepsilon_{H^+}^M + \varepsilon_{H_2O}^M + \varepsilon_{CH_3OH}^M \tag{T2.16}$$

Phase equilibrium (AC-ACP)

$$\varepsilon_{CH_3OH}^{ACP} = 25.4831(x_{CH_3OH}^{AC})^3 + 4.2821(x_{CH_3OH}^{AC})^2 1.6354 x_{CH_3OH}^{AC} \tag{T2.7}$$

$$\varepsilon_{H_2O}^{ACP} = 104.9956(x_{CH_3OH}^{AC})^3 + 20.9052(x_{CH_3OH}^{AC})^2$$

$$+ 2.6349 x_{CH_3OH}^{AC} + 0.4601 \tag{T2.8}$$

Phase equilibrium (CC-CCP)

$$\Lambda^{CCP} = \frac{N_{H_2O}^M}{N_{R-SO_3^-}} = 28.5(a_{H_2O(g)}^{*,CC} - 0.35)^3 + 5(a_{H_2O(g)}^{*,CC} - 0.35) + 3$$

with $a_{H_2O(g)}^{*,CC} = \frac{p_{H_2O}^{CC}}{p_{H_2O}^{\text{sat}}(T^{CC})}$ (T2.17)

Table 3

Model equations and parameters of models I, IIa/b and III (both catalyst layers)

Components	Model I: anode catalyst layer (AC)	Model I/model II: cathode catalyst layer (CC)
	Index j = H$_2$O, CH$_3$OH, CO$_2$ (pure liquid phase)	Index j = N$_2$, O$_2$, H$_2$O, CO$_2$ (pure gas phase)
Reaction mechanism	CH$_3$OH + H$_2$O $\overset{PtRu,r_a}{\longleftrightarrow}$ CO$_2$ + 6H$^+$ + 6e$^-$ (T3.1)	1.5O$_2$ + 6H$^+$ + 6e$^-$ $\overset{pt,r_c}{\longrightarrow}$ 3H$_2$O (T3.12)
		CH$_3$OH + 0.5O$_2$ $\overset{pt,r_{cross}}{\longrightarrow}$ CO$_2$ + 4H$^+$ + 4e$^-$ (T3.13)
Component mass balance	$\dfrac{dc_j^{AC}}{dt} = \dfrac{n_j^{AD}\vert_{z_{AD}=d^{AD}} - n_j^{M}\vert_{z_M=0}}{\varepsilon_{pores}^{AC} d^{AC}} + \nu_{a,j} r_a$ (T3.2)	$\dfrac{dc_j^{CC}}{dt} = \dfrac{n_j^{M}\vert_{z_M=d^M} - n_j^{CD}\vert_{z_{CD}=0}}{\varepsilon_{pores}^{CC} d^{CC}} + \nu_{c,j} r_c + \nu_{cross,j} r_{cross}$ (T3.14)
Stoichiometric constants	$\nu_{a,CH_3OH} = -1$; $\nu_{a,H_2O} = -1$; $\nu_{a,CO_2} = +1$	$\nu_{c,O_2} = -1.5$; $\nu_{c,N_2} = 0$; $\nu_{c,H_2O} = +3$; $\nu_{c,CO_2} = 0$; $\nu_{cross,O_2} = -0.5$; $\nu_{cross,N_2} = 0$; $\nu_{cross,H_2O} = 0$; $\nu_{cross,CO_2} = +1$
Charge balance	$0 = i_{cell} - i^{M}\vert_{z_M=0}$ with $i_{cell} = i_a = d^{AC}\varepsilon_{pores}^{AC} 6F r_a$ (T3.3)	$0 = i_{cell} - i^{M}\vert_{z_M=d^M}$ with $i_{cell} = (i_{cross} + i_c)$; $i_c = d^{CC}\varepsilon_{pores}^{CC} 6F r_c$; $i_{cross} = d^{CC}\varepsilon_{pores}^{CC} 4F r_{cross}$ (T3.15)
Rate expressions	$r_a = k_a \left[x_{CH_3OH}^{AC} \exp\left(\dfrac{\alpha_a 6F}{RT^{AC}}\eta_a - x_{CO_2}^{AC} \exp\left(-\dfrac{(1-\alpha_a)6F}{RT^{AC}}\eta_a \right) \right) \right]$ with $\alpha_a = 0.1$, $k_a = 6\times 10^{-3}$ mol m^{-3} s^{-1} (T3.4)	$r_c = k_c \left[\left(\dfrac{p_{O_2}^{CC}}{10^5 pa} \right)^{1.5} \exp\left(-\dfrac{\alpha_c 6F}{RT^{CC}}\eta_c \right) - \exp\left(-\dfrac{(1-\alpha_c)6F}{RT^{CC}}\eta_c \right) \right]$ (T3.16) model I, IIa: $\alpha_c = 0.5$, $k_c = 1.27\times 10^{-21}$ mol m^{-3} s^{-1}; model IIb: $\alpha_c = 0.905$, $k_c = 2.7\times 10^{-2}$ mol m^{-3} s^{-1} $r_{cross} = \dfrac{n_{CH_3OH}^{M}\vert_{z_M=d^M}}{d^{CC}\varepsilon_{pores}^{CC}}$ (T3.17)

Components	Model II/model III: anode catalyst layer (AC)	Model III: cathode catalyst layer (CC)
	Index j = H$_2$O, CH$_3$OH, CO$_2$ (pure liquid phase)	Index j = N$_2$, O$_2$, H$_2$O, CO$_2$ (pure gas phase)
Reaction mechanism	CH$_3$OH + Pt $\overset{r_{a1}}{\longrightarrow}$ PtCO + 4H$^+$ + 4e$^-$ (T3.5) PtCO + H$_2$O $\overset{Ru,r_{a2}}{\longrightarrow}$ CO$_2$ + 2H$^+$ + 2e$^-$ + Pt (T3.6)	0.5O$_2$ + Pt $\overset{r_{c1}}{\longrightarrow}$ PtO (T3.18) PtO + 2H$^+$ + 2e$^-$ $\overset{-r_{c2}}{\longrightarrow}$ Pt + H$_2$O$\sqrt{2}$ (T3.19) CH$_3$OH + Pt $\overset{r_{c3}}{\longrightarrow}$ PtCO + 4H$^+$ + 4e$^-$ (T3.20) PtO + PtCO $\overset{r_{c4}}{\longrightarrow}$ 2Pt + CO$_2$ (T3.21)
Component mass balance	$\dfrac{dc_j^{AC}}{dt} = \dfrac{n_j^{AD}\vert_{z_{AD}=d^{AD}} - n_j^{M}\vert_{z_M=0} \nu_{a1,j} r_{a1} + \nu_{a2,j} r_{a2}}{\varepsilon_{pores}^{AC} d^{AC}}$ (T3.7) $\dfrac{d\Theta_{CO}^{AC}}{dt} = \dfrac{r_{a1} - r_{a2}}{\hat{N}_{pt}^{AC}}$ with $\hat{N}_{pt}^{AC} = 0.11$ mol m^{-2} (T3.8)	$\dfrac{dc_j^{CC}}{dt} = \dfrac{n_j^{M}\vert_{z_M=d^M} - n_j^{CD}\vert_{z_{CD}=0}}{\varepsilon_{pores}^{AC} d^{CC}} \displaystyle\sum_{k=1}^{4} \nu_{ck,j} r_{ck}$ (T3.22) $\dfrac{d\Theta_{CO}^{CC}}{dt} = \dfrac{r_{c3} - r_{c4}}{\hat{N}_{pt}^{CC}}$ (T3.23) $\dfrac{d\Theta_{O}^{CC}}{dt} = \dfrac{r_{c1} + r_{c2} - r_{c4}}{\hat{N}_{pt}^{CC}}$ with $\hat{N}_{pt}^{CC} = 0.11$ mol m^{-2} (T3.24)
Stoichiometric constants	$\nu_{a1,CH_3OH} = -1$; $\nu_{a1,H_2O} = 0$; $\nu_{a1,CO_2} = 0$; $\nu_{a2,CH_3OH} = 0$; $\nu_{a2,H_2O} = -1$; $\nu_{a2,CO_2} = +1$	all $\nu_{ck,j} = 0$ except for : $\nu_{c1,O_2} = -0.5$; $\nu_{c2,H_2O} = -1$; $\nu_{c4,CO_2} = +1$
Charge balance	$0 = i_{cell} - i^{M}\vert_{z_M=0}$ with $i_{cell} = i_{a1} + i_{a2} = 4F r_{a1} + 2F r_{a2}$ (T3.9)	$0 = i_{cell} - i^{M}\vert_{z_M=d^M}$ with $i_{cell} = -i_{c3} - i_{c2}$; $i_{c2} = d^{CC}\varepsilon_{pores}^{CC} 2F r_{c2}$; $i_{c3} = d^{CC}\varepsilon_{pores}^{CC} 4F r_{c3}$ (T3.25)
Rate expressions	$r_{a1} = k_{a1} \dfrac{C_{CH_3OH}^{AC}}{C_{CH_3OH}^{ref}} \dfrac{1-\Theta_{CO}}{1-\Theta_{CO}^{ref}} \exp\left(\dfrac{\alpha_{a1}F}{RT^{AC}}\eta_a \right)$ (T3.10) $r_{a2} = k_{a2} \dfrac{c_{CO}^{AC}}{c_{CO}^{ref}} \exp\left(\dfrac{\alpha_{a2}F}{RT^{AC}}\eta_a \right)$ (T3.11) with $\alpha_a = 0.5$, $\Theta_{CO}^{ref} = 0.5$, $C_{CH_3OH}^{ref} = 1000$ mol m^{-3}, $k_{a1} = 1.6\times 10^{-3}$ mol m^{-2} s^{-1}, $k_{a2} = 8\times 10^{-5}$ mol m^{-2} s^{-1}	$r_{c1} = k_{c1} \left(\dfrac{p_{O_2}^{CC}}{p_{O_2}^{ref}} \right)^{0.5} (1 - \Theta_{CO} - \Theta_O)$ (T3.26) $r_{c2} = -k_{c2}\Theta_O \exp\left(-\dfrac{(1-\alpha_{c2})F}{RT^{CC}}\eta_c \right)$ (T3.27) $r_{c3} = \dfrac{n_{CH_3OH}^{M}\vert_{z_M=d^M}}{d^{CC}\varepsilon_{pores}^{CC}}$ (T3.28) $r_{c4} = k_{c4}\Theta_O\Theta_{CO} \exp\left((1-\beta_{CO})f_{CO}(\Theta_{CO} - \Theta_{CO}^{ref}) \right)$ (T3.29) with $\alpha_{c2} = 0.5$, $\Theta_{CO}^{ref} = 0.5$, $p_{O_2}^{ref} = 10^5$ Pa, $k_{c1} = 3.4\times 10^3$ mol m^{-3} s^{-1}, $k_{c2} = 1\times 10^{-1}$ mol m^{-3} s^{-1}, $k_{c4} = 7.1\times 10^3$ mol m^{-3} s^{-1}, $\beta_{c0} = 0.5$, $f_{c0} = 10$

account for the influence of the surface coverage of the platinum catalyst with adsorbed CO (Langmuir adsorption/desorption kinetics).

The cathode in model II is identical to that in model I.

3.3. Model III: extended cathode kinetics with adsorbed CO and O

On the cathode platinum catalyst, very similar processes as on the anode side take place with respect to the methanol, which crosses over through the PEM. Therefore it seems appropriate to use similar reaction schemes and rate expressions like the ones formulated in model II for the anode side.

It is assumed, that oxygen and methanol compete for the free platinum catalyst surface (Table 3, lower right quarter): oxygen is adsorbed in a non-electrochemical reaction forming Pt-O (Eq. T3.18), methanol is adsorbed forming Pt-CO, as well as protons and electrons (Eq. T3.19). Both steps are assumed to be fast. The adsorbed oxygen (Pt-O) can then take up protons and electrons to form free platinum sites and water (Eq. T3.20). In parallel, Pt-CO reacts with Pt-O to carbon dioxide and free platinum sites (Eq. T3.21).

Based on this reaction scheme, both surface species (Pt-O and Pt-CO) have to be balanced (Θ_O^{CC}, Eq. T3.23 and Θ_{CO}^{CC}, Eq. T3.24), and the contributions of both electrochemical reactions are considered in the charge balance (Eq. T3.25). The rate expression of the first reaction (Eq. T3.26) is of Langmuir type (non-electrochemical irreversible adsorption), the electrochemical oxygen reduction is formulated as combined Langmuir–Tafel kinetics (Eq. T3.27, analogue to the anode side). The methanol adsorption is assumed to be an immediate reaction, therefore its rate (Eq. T3.28) is proportional to the methanol crossover flux density (as in the previous models). Finally, the release of carbon dioxide is described by an irreversible Temkin–Frumkin desorption kinetics (Eq. T3.29).

The anode in model III is the same as in model II.

4. Simulation results

In this section, in a first step the presented model variants are compared to the experimental results. In a second step, model III is examined more closely for varying operating conditions (in terms of cell temperature and cell current density).

4.1. Comparison of model variants

For the operating conditions given in Section 2 and a cell current density of $56\,\mathrm{mA\,cm^{-2}}$, the model variants yield cell voltage predictions as presented in Fig. 5. It can be seen that model I predicts the cell breakdown much earlier than what was found in the experiments, while all other models predict the sustaining time correctly. Model II can also predict cell voltage overshoots, if the cathode charge transfer coefficient is set to the relatively high value of $\alpha_c = 0.905$ (model IIb). Model III finally can predict overshoots with charge transfer coefficients of 0.5 on both anode and cathode side. All kinetic parameters used in the model variants are given in Table 3.
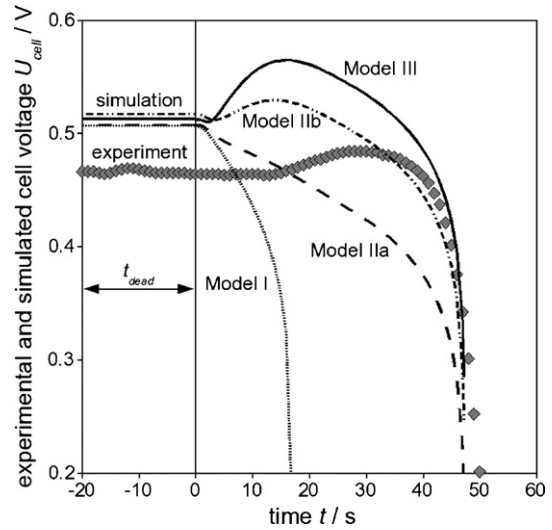
Fig. 5. Comparison of simulated and experimental cell voltages (operating conditions as in Section 2, cell current density $i_{cell} = 56\,\mathrm{mA\,cm^{-2}}$).

The high value for the cathode charge transfer coefficient in model IIb is a strong hint that in the cathode reaction, adsorption processes play a major role, justifying the formulation of a more complex cathode kinetics like that in model III.

A more detailed insight in the underlying physico-chemical processes can be obtained by a closer look at the state variables and the methanol crossover flux densities of the model variants as presented in Fig. 6 (anode side) and Fig. 7 (cathode side). In Fig. 6, the anode catalyst layer state variables (methanol concentration $c_{CH_3OH}^{AC}$, surface coverage on the Pt catalyst Θ_{CO}^{AC}, overpotential η_a) and the methanol crossover flux density $n_{CH_3OH}^M|_{z^M=0}$ at the interface between anode catalyst layer and PEM ($z^M = 0$) are plotted over time.
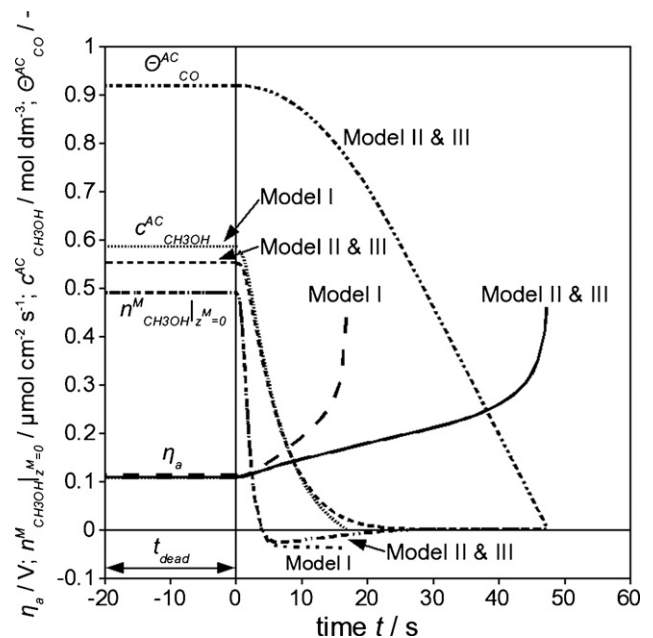
Fig. 6. Comparison of simulation results (anode side) of model variants (operating conditions as in Section 2, cell current density $i_{cell} = 56\,\mathrm{mA\,cm^{-2}}$).
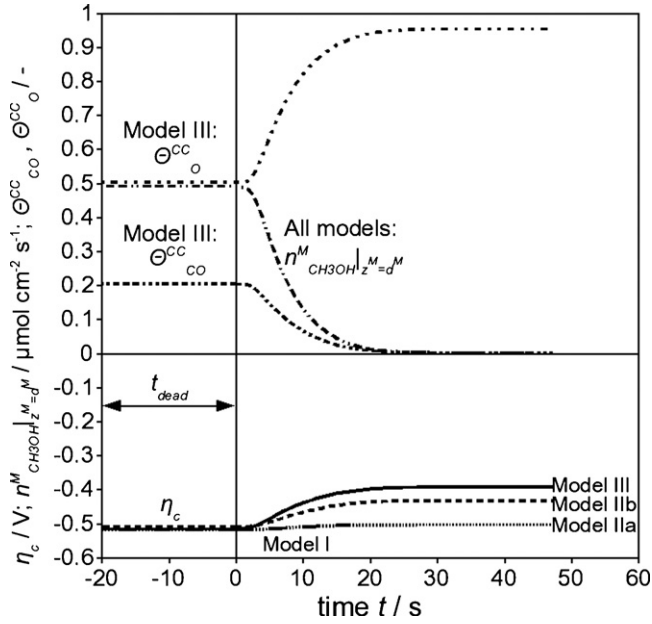
Fig. 7. Comparison of simulation results (cathode side) of model variants (operating conditions as in Section 2, cell current density $i_{cell} = 56\,\text{mA cm}^{-2}$).

One can see that the variables related to (methanol) mass transport ($c_{CH_3OH}^{AC}$ and $n_{CH_3OH}^{M}$) yield very similar results for all three models (Fig. 6). This could be expected, as the model variants only differ with regard to the assumed electrode kinetics. All models predict a fast decrease of the methanol concentration in the anode catalyst layer ($c_{CH_3OH}^{AC}$), slightly (but almost negligibly) slowed down by a small reflux of methanol from the membrane back into the anode catalyst layer ($n_{CH_3OH}^{M} > 0$: methanol flux towards cathode, $n_{CH_3OH}^{M} < 0$: methanol flux towards anode). Less than 20 s after the feed switch in all cases no more unreacted methanol is available as reactant for the anode reactions.

As model I has no other reactant storages, its anode overpotential then sharply increases leading to an immediate breakdown of the cell voltage (Fig. 6). In the other model variants (II/III), the cell can be operated beyond the point where the unreacted methanol in the anode catalyst layer is depleted, as carbon monoxide (CO) adsorbed to the platinum catalyst forms another reactant reservoir. Only when this storage (described by the CO surface coverage Θ_{CO}^{AC}) is empty as well, the anode overpotential finally increases sharply. Moreover, between the feed switch and the final cell breakdown the anode overpoten-
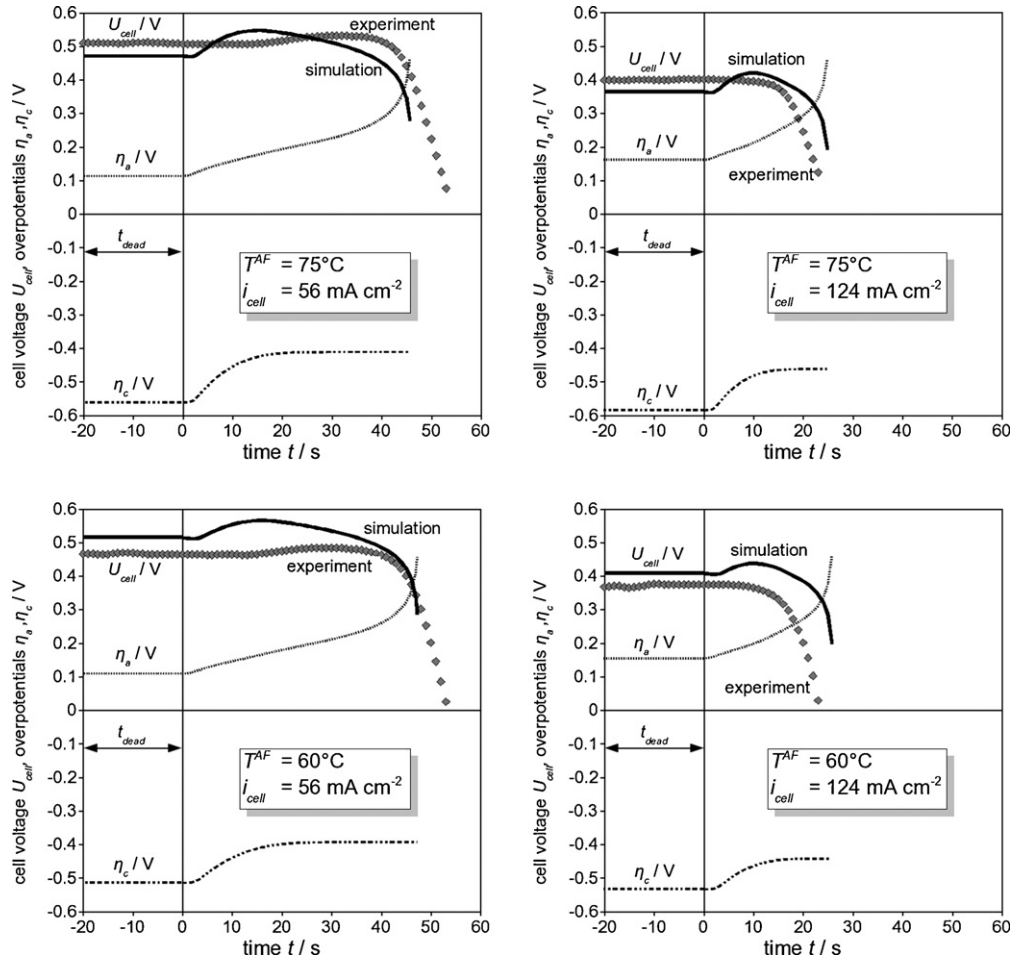
Fig. 8. Comparison of simulation results of model III to experimental data (operating conditions as in Section 2, except for cell current density i_{cell} and anode feed temperature T^A).
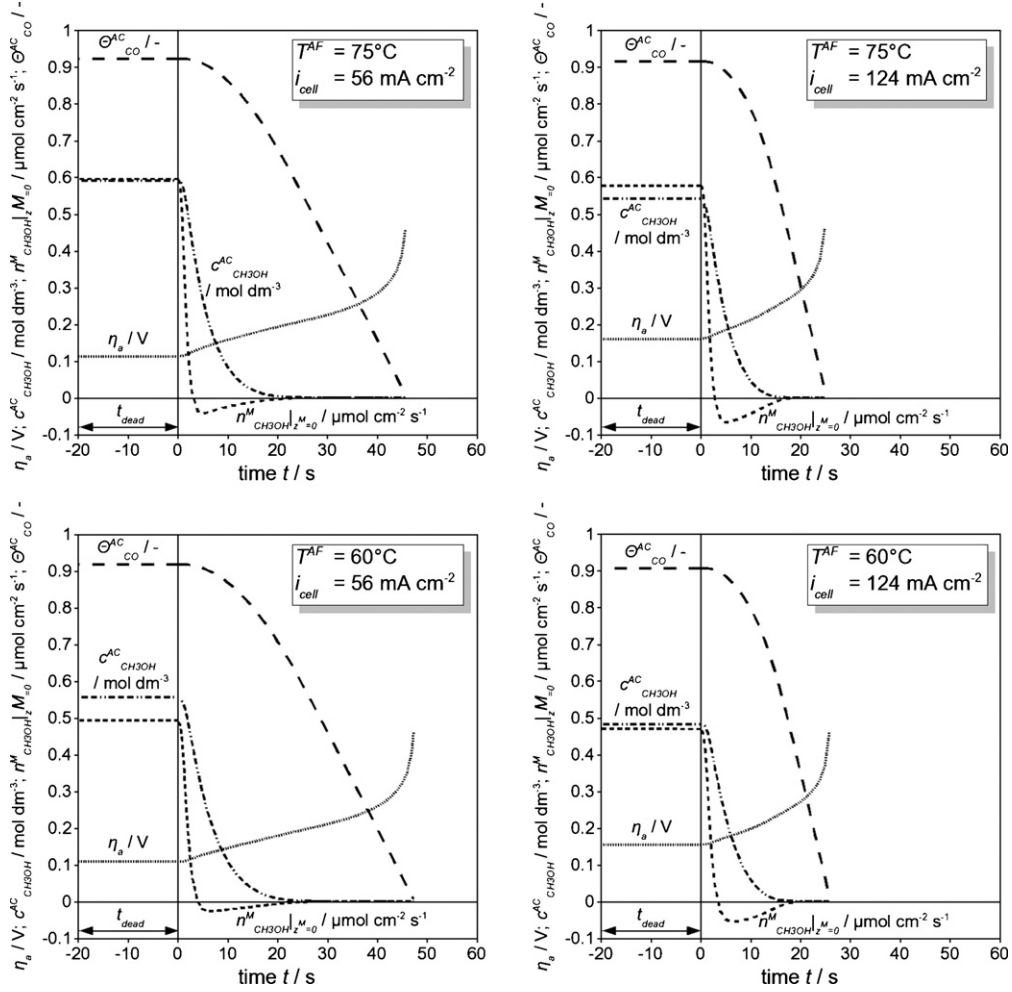
Fig. 9. Comparison of simulation results of model III (anode side) (operating conditions as in Section 2, except for cell current density i_{cell} and anode feed temperature T^A).

tial in models II and III also increases much slower than in model I.

Fig. 7 presents the cathode catalyst layer state variables and methanol crossover flux density at the interface between PEM and cathode catalyst layer ($z^M = d^M$) of the model variants. Like on the anode side, also here the models do not differ significantly in terms of mass transport. A few seconds after the feed switch, the methanol crossover flux reaching the cathode catalyst ($n^M_{CH_3OH}|_{Z^M=d^M}$) begins to decrease, and with it the absolute value of the cathode overpotential. Roughly 20 s after the feed switch (i.e. when the methanol concentration in the anode catalyst layer, $c^{AC}_{CH_3OH}$, has dropped to zero), the methanol crossover flux has ceased completely, and the cathode overpotential reaches a new steady state value. The decreasing methanol crossover also leads to a parallel decrease of the cathode CO coverage (Θ^{CC}_{CO}) in model III, while the oxygen coverage of the cathode catalyst (Θ^{CC}_O) is increasing accordingly, taking over the sites freed from CO. Obviously, all model variants' cathode processes react with the same time constant, they differ only in the steady state overpotentials. Therefore, for a simple model, the original cathode model with lumped Butler–Volmer type rate expression (Table 3,

T3.12–T3.17) with appropriately fitted parameters (model IIb) is sufficient.

It is obvious from Figs. 6 and 7, that in order to achieve a cell voltage overshoot after the feed switch, the slope of the cathode overpotential has to be larger than the slope of the anode overpotential. As soon as the cathode arrives at its new steady state, the cell voltage reaches its maximum, and then declines due to the continuing increase of the anode overpotential.

It can be seen that models IIb and III predict the maximum of the overshoot earlier than what is observed in the experiments (Fig. 5). The result would be better if the dead time t_{dead} accounted for in the experiments would be larger than the estimated 20 s. In fact, this estimation might be too low, as in the first seconds after the feed switch the experimental setup is in a somewhat transitional state, slowly readjusting anode pressure and flow rate, while t_{dead} was estimated assuming constant flow rate without interruptions (see Section 2). The measured cell voltage curves (Figs. 1–3) could also support a somewhat longer dead time t_{dead} of up to 25–30 s.

Nonetheless, such an additional experimental time delay cannot fully explain the deviations between times at which the maxima of the overshoots are reached in the simulations and the
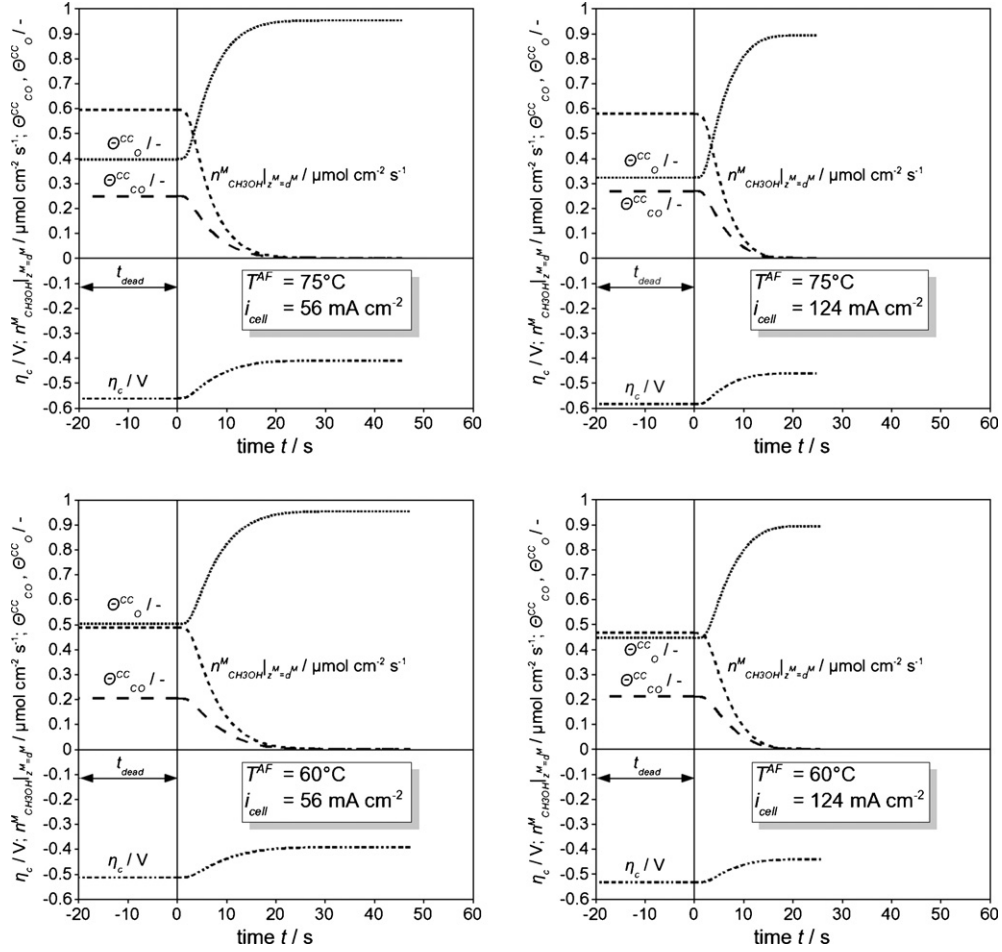
Fig. 10. Comparison of simulation results of model III (cathode side) (operating conditions as in Section 2, except for cell current density i_{cell} and anode feed temperature T^A).

experiments. On one hand, the time constant of the methanol crossover might be too low in the models: in this case the transport coefficients for methanol in the PEM need to be adjusted. On the other hand, the cathode overpotential might be less dependent on the methanol crossover flux: this could be accounted for by adjusting the cathode rate constants, and/or the rate expression for the electrochemical step (r_{c2}, Table 3, T3.27).

4.2. Analysis of model III for different operating conditions

Figs. 8–10 present simulation results from model III for two different anode feed temperatures ($T^{AF} = 60$, $75\,°C$) and two different current densities ($i_{cell} = 56$, and $124\,mA\,cm^{-2}$). Fig. 8 compares cell voltages and overpotentials, Fig. 9 compares the most important anode state variables and mass fluxes, while Fig. 10 does the same for the cathode side. The following observations and resulting conclusions can be summarized.

4.2.1. Observation (1)

The time till the cell breaks down is predicted almost correctly by the model (Fig. 8). This is a proof, that the sum of internal reactant storages (which are responsible for the sustained operability after the cut off supply of fresh methanol) is

quite realistic. Nonetheless, this observation does not give any hints on the type and quality of different reactant storages.

4.2.2. Observation (2)

The breakdown of the cell voltage is predicted more steeply than what was found in the experiments (Fig. 8). In the simulations the final breakdown slopes of the cell voltage are given by the slopes of the respective anode overpotentials. Therefore, the model descriptions of the underlying phenomena (transport of methanol to the anode as well as anode reaction mechanism and reaction rates, Fig. 9) might need some further refinement.

4.2.3. Observation (3)

The maxima of the overshoots are predicted too early, and the relative overshoots w.r.t. the initial steady state are predicted higher than what was found in the experiments (Fig. 8). In the simulation, the different behaviour of both the anode and cathode overpotentials (i.e. their time constants) is responsible for the overshoots, as can be seen from Fig. 8. The maximum cell voltage is reached when the cathode overpotential has reached its new steady state due to the ceasing methanol crossover. Obviously, if the methanol crossover ($n^M_{CH_3OH}|_{Z^M=d^M}$ in Fig. 10) faded more slowly, the maximum of the overshoot would appear

later, and presumably be also less pronounced. Therefore it might be beneficial to check the transport properties of the model (in the PEM and in the anode diffusion layer), as well as whether the experimental dead time is correct (see above sections). If in the model the transport of methanol within the anode diffusion layer (AD) should be slower due to accounting for the blockage of pores by carbon dioxide gas, $c_{CH_3OH}^{AC}$ would decrease slower leading to a slower decrease in the methanol crossover and thus also in the absolute value of the cathode overpotential. The same would be true if the methanol transport inside the PEM was slightly slower. As the neglection of a carbon dioxide gas phase in the anode pore structures is a significant model simplification compared to the real situation, it can be assumed that this is the main reason for the presumably too fast decrease of the methanol concentration in the anode catalyst layer. In any case, if model adjustments on the mass transport side should be necessary, the internal reactant storages (especially the number of adsorption sites on the anode catalyst, $\hat{N}_{Pt}^{AC}$) would have to be slightly reduced to achieve the same overall breakdown times as in the present simulations.

4.2.4. Observation (4)

The model predicts cell voltage overshoots for all four cases shown in Figs. 8–10, but in the experiments for the higher cell current density ($i_{cell} = 124\,mA\,cm^{-2}$) no overshoots were observed. Nonetheless, the model predicts the relative height of the overshoots to decrease with increasing current density. Adjusting the rate constants can decrease the overshoots in general, therefore a disappearance for high current densities seems possible. To correctly predict the experimental behaviour for the higher current density, the absolutes of the slopes of the cathode and anode overpotentials, respectively, after the feed switch would have to be identical. Then the cell voltage would remain constant till the cathode overpotential approaches its new steady state, while the anode overpotential would still increase, thus leading to a breakdown of the cell voltage in the observed manner.

4.2.5. Observation (5)

Finally, from the steady state simulation results prior to the feed switch, one can see that the model predicts an increase of the cell voltage with higher cell temperature, while in the experiments a contrary behaviour is observed (Fig. 8). In the presented model, the rate constants are fitted for an anode feed temperature of $60\,^{\circ}C$, no additional (Arrhenius) term accounts for changes in the reaction rate constants with temperature (see Table 3, rate Eqs. T3.4, T3.10, T3.11, T3.16 and T3.26–T3.29). A modification of the rate constants by introducing such an Arrhenius term will be part of the next steps in model refinement. For the anode side, the additional parameters (activation energies) have been determined from experiments recently [8].

5. Conclusions

The dynamic response of the DMFC to step changes in the anode feed methanol concentration was analysed experi-

mentally, and a dynamic process model was formulated. The experiments revealed, that for switching the feed from methanol solutions to pure water the cell voltage breaks down later than expected, and for low current densities even shows an overshoot behaviour.

The here presented model shows good quantitative agreement to steady state experiments, and also a good qualitative agreement to the aforementioned dynamic step-down experiments (long sustaining times and overshoots of the cell voltage).

According to the model analysis, the overshoot phenomenon can be explained by different response times (time constants) of the anode and cathode overpotentials, respectively. After rinsing the anode compartment, the methanol concentration in the anode catalyst layer drops rapidly due to the ongoing methanol consumption by the electrochemical reactions and methanol transport towards the anode compartment. Consequently, the methanol crossover to the cathode decreases, leading to a decrease of the absolute cathode overpotential. The anode overpotential increases quite slowly, and the cell voltage does not break down when the reactant methanol is completely consumed. The latter is due to reaction intermediates of the anodic methanol oxidation adsorbed to the anode catalyst (e.g. CO), which form a second reactant reservoir. This enables a prolonged operation of the cell for a few seconds up to a few 10 s (depending on current density).

The reason for the observed overshoots therefore seems to be, that the absolute cathode overpotential (mainly determined by methanol crossover) decreases faster, than the anode overpotential increases in this transient situation.

The analysis has also revealed several hints for further model improvement:

- More realistic anode diffusion layer mass transport accounting for the influence of carbon dioxide gas bubbles blocking part of the available pores.
- Validation of the experimental dead time.
- Adjustment of reaction rate expressions and corresponding parameters.

On the other hand it can be concluded, that for a reduced model it might be sufficient to use a simplified cathode reaction mechanism (as in model I/II) with Butler–Volmer or even Tafel type rate expressions. Nonetheless, a realistic anode reaction mechanism (e.g. models II/III), seems to be necessary in order to correctly predict the dynamic DMFC behaviour.

References

[1] T. Schultz, Experimental and model-based analysis of the steady state and dynamic operating behaviour of the direct methanol fuel cell (DMFC), Dissertation thesis, Otto-von-Guericke University Magdeburg, 2004.

[2] K. Sundmacher, K. Scott, Chem. Eng. Sci. 54 (1999) 2927–2936.

[3] T. Schultz, K. Sundmacher, J. Power Sources 145 (2005) 435–462.

[4] T. Schultz, K. Sundmacher, J. Membr. Sci. 276 (2005) 272–285.

[5] A.S. Arico, S. Srinivasan, V. Antonucci, Fuel Cells 1 (2) (2001) 133–161.

[6] S. Zhou, T. Schultz, M. Peglow, K. Sundmacher, Phys. Chem. Chem. Phys. 3 (3) (2001) 347–355.

[7] K. Sundmacher, T. Schultz, S. Zhou, K. Scott, M. Ginkel, E.D. Gilles, Chem. Eng. Sci. 56 (2001) 333–341.

[8] T. Vidakovic, M. Christov, K. Sundmacher, J. Electroanal. Chem. 580 (2005) 105–121.

[9] U. Krewer, M. Christov, T. Vidakovic, K. Sundmacher, J. Electroanal. Chem. 589 (2006) 148–159.